We are IntechOpen, the world's leading publisher of Open Access books Built by scientists, for scientists

4,800
Open access books available

122,000
International authors and editors

135M
Downloads

Our authors are among the

154
Countries delivered to

TOP 1%
most cited scientists

12.2%
Contributors from top 500 universities

WEB OF SCIENCE™

Selection of our books indexed in the Book Citation Index in Web of Science™ Core Collection (BKCI)

Interested in publishing with us?
Contact book.department@intechopen.com

Numbers displayed above are based on latest data collected.
For more information visit www.intechopen.com

7

$KTiOPO_4$ single nanocrystal for second-harmonic generation microscopy

Loc Le Xuan, Dominique Chauvat, Abdallah Slablab and Jean-Francois Roch
Ecole Normale Superieure de Cachan
France

Pawel Wnuk and Czeslaw Radzewicz
University of Warsaw
Poland

1. Introduction

Nonlinear second-harmonic generation (SHG) microscopy has become a commonly used technique for investigating interfacial phenomena(Kemnitz et al., 1986; Shen, 1989) and imaging biological samples.(Moreaux et al., 2000) Different non-centrosymmetric nanometric light sources have been recently studied in this context, e.g. organic nanocrystals.(Shen et al., 2001; Treussart et al., 2003) For those systems, resonant optical interaction leads to an enhancement of the nonlinear response but also to parasitic effect that is detrimental for practical applications, namely photobleaching due to two-photon residual absorption.(Patterson et al., 2000) Conversely, inorganic non-centrosymmetric materials with far-off resonance interaction avoid this limitation.(Johnson et al., 2002; Long et al., 2007) Recent achievements have been obtained using $KNbO_3$ nanowires as a tunable source for sub-wavelength optical microscopy(Nakayama et al., 2007) and $Fe(IO_3)_3$ nanocrystallites as promising new SHG-active particles with potential application in biology.(Bonacina et al., 2007) However, either the dimensions of the used crystals are still of the order of the micrometer along one axis,(Nakayama et al., 2007) or the corresponding bulk material is not easily grown,(Bonacina et al., 2007) so that the crystal characteristics are not directly available. A complementary approach consists in considering a well-known SHG-active bulk material and investigating its properties in nanoparticle form. Different materials have been considered, e.g. BaTiO3 (Hsieh et al., 2009) and ZnO (Kachynski et al., 2008). In this view, we were among the pioneers in this domain, considering the well-known KTP material. Potassium titanyl phosphate ($KTiOPO_4$, KTP) is a widely used nonlinear crystal.(Zumsteg et al., 1976) Studies on this material have focused on the optimized growth of large-size single crystals, which have found numerous applications in laser technology for efficient frequency conversion.(Driscoll et al., 1986)

Here we show that KTP particles of nanometric size (nano-KTPs) are an attractive material for SHG microscopy. Under femtosecond excitation and in ambient conditions, a single nano-KTP with a size around 60 nm independently determined with atomic force microscopy (AFM), generates a perfectly stable blinking-free second-harmonic signal which can be easily detected in the photon-counting regime. Furthermore, we demonstrate that this single nanocrystal can

be characterized in situ by retrieving the orientation of its 3-axis with respect to the optical observation axis. This analysis uses both nonlinear polarimetry(Brasselet et al., 2004) and defocused imaging with a model that has been adapted from similar techniques developed for single-molecule fluorescence.(Bohmer & Enderlein, 2003; Brokmann et al., 2005; Sandeau et al., 2007)
Such characterized nanocrystal can have potentially many applications in nano-optics or biology, and downscaling their size is a crucial step forward. From the point of view of detection techniques, we have developed two methods for investigating SHG nanocrystals and decrease the minimum detectable size for a SHG nanocrystal. In particular both techniques exploit the coherent characteristics of the second harmonic emission. First, a coherent balanced homodyne detection is associated to SHG microscopy, allowing us to detect nano-objects with high signal-to-noise ratio and phase sensitivity.(Le Xuan et al., 2006) Second, broadband femtosecond pulses are used to improve the second harmonic signal, with a perspective of spectral manipulation for coherent control of the nonlinear process.(Wnuk et al., 2009)

2. Photostable second harmonic generation from single KTP nanocrystals

The KTP nanoparticles are extracted from the raw powder that remains in the trough at the end of the flux-growth process which leads to the synthesis of large sized KTP single crystals.(Rejmankova et al., 1997) We then apply a size-selection procedure by centrifugation which was previously worked out for optically active nanodiamonds (Treussart et al., 2006) and which leads to a colloidal solution of non-aggregated particles.
Analysis with dynamic light scattering (DLS) of this solution reveals a strong peak in the size distribution centered around 150 nm (Fig.1). Centrifugation at a higher speed or for a longer duration acts as a low-pass filter on the size distribution, reducing the average peak value from 150 nm to 80 nm (30 min. at 5000 rpm), and 60 nm (10 min. at 11000 rpm).

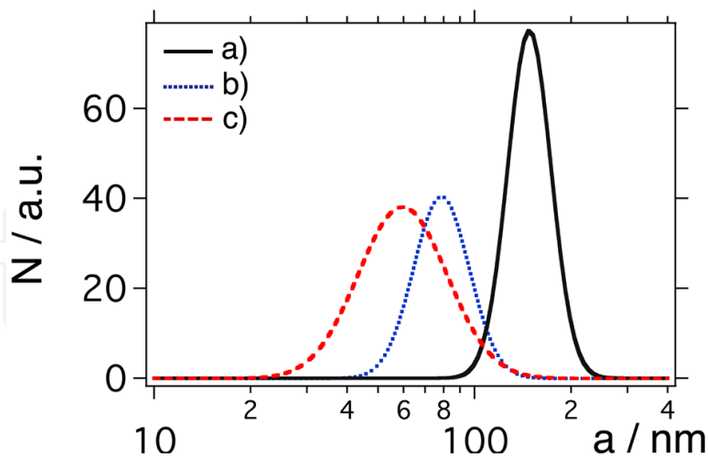

Fig. 1. Size selection of the nanoparticles in the polymer solution. DLS spectra for successive centrifugations (a) 5 min. at 5000 rpm, (b) 30 min. at 5000 rpm, (c) 10 min. at 11000 rpm, and corresponding to an average particle size of (a) 150 nm, (b) 80 nm, (c) 60 nm.

Since we are interested in the study of a well-isolated single nanocrystal, the sample is prepared so as to enable identification of the same single nano-object under AFM, a classical white-light optical microscope, and a home-made scanning SHG microscope (Figure 2). We

designed structured samples by first spin-coating the colloidal solution on a glass cover-slip, then etching it through a mask to leave square areas with nano-KTPs directly on glass. Figure 3a shows one such area labeled with photo-written numbers by the focus laser itself at high mean power (100mW at a repetition rate of 86MHz) and imaged using transmission microscopy in white-light illumination. Figure 3b corresponds to a $10\times10\ \mu m^2$ zoom inside this domain. Well-contrasted spots are clearly visible and are attributed to the strong elastic scattering from nano-KTPs resulting from the mismatch between the index of refraction of glass (n $\approx$ 1.5 in the visible spectrum) and the average one of KTP (n $\approx$ 1.8). Figure 3c is an AFM image of exactly the same domain taken in non-contact operation mode. It indeed reveals a large number of objects with nanometric size.

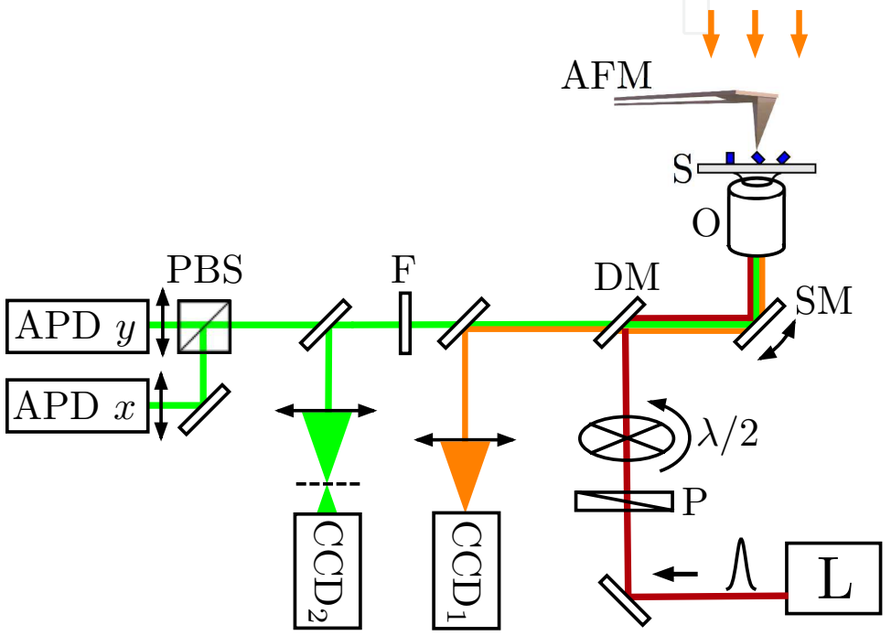

Fig. 2. Experimental setup. AFM: atomic force microscope mount on top of the optical set-up. L: femtosecond laser (86 MHz repetition rate, $\approx$ 100 fs pulse duration, $\lambda = 986$ nm), P: polarizer, $\lambda/2$ half-wave plate, DM: dichroic mirror, SM: scanning mirror, O: microscope objective (N.A. = 1.40, $\times$ 100), S: sample, CCD_1 white-light camera, CCD_2 sesitive CCD camera, PBS: polarization beam splitter, APD: avalanche photodiode functioning in photo-counting regime

KTP is a non-centrosymmetric orthorhombic crystal with large nonlinear coefficients, of the order of $\chi^{(2)}_{zzz} = 2d_{33} \approx 34$ pm/V along its 3-axis, when excited in the near infrared.(Sutherland, 1996) We use a SHG microscope, as described in Figure 2, to identify if the scattering objects identified in Figures. 3a an 3b correspond to optically-active particles with nonlinear response. Femtosecond infrared light pulses (100 fs) at 86 MHz repetition rate are tightly focused on the sample with a high numerical aperture microscope objective (NA=1.4, $\times$100). Since the nanocrystal size is much smaller than the wavelength, we can neglect any phase shift between the fundamental and second-harmonic fields. Compared to propagation in a bulk nonlinear crystal, there is no phase-matching requirement, thus allowing us to excite the nanocrystal at any wavelength. Here we choose the excitation wavelength

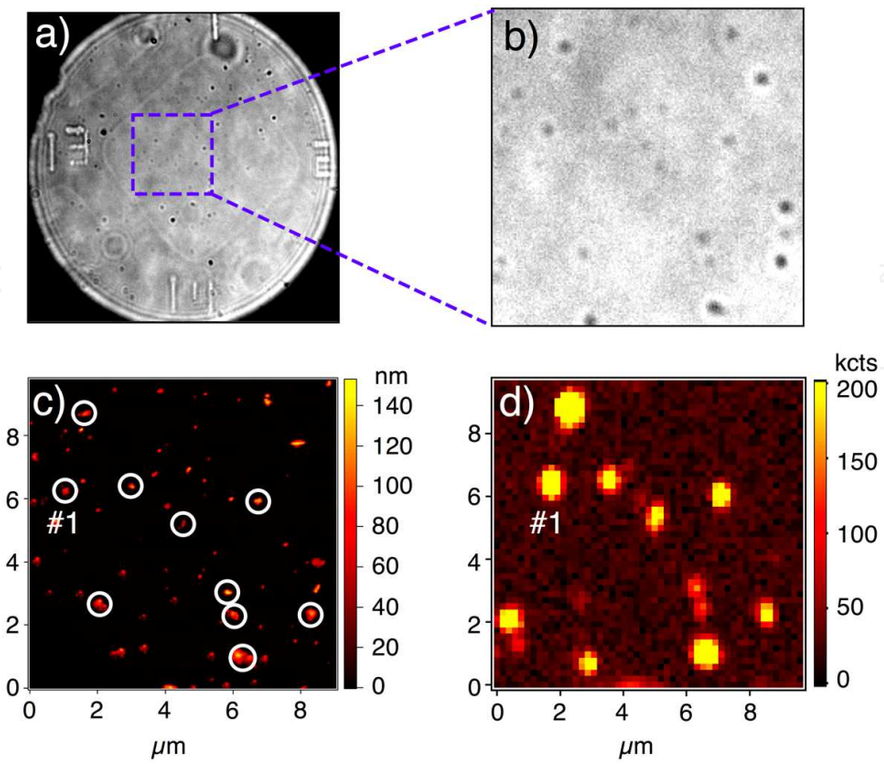

Fig. 3. Correspondence of nanoparticles in images taken with different observational techniques. (a) Overview in white-light microscopy of the structured sample. The image displays a square area with nano-KTPs deposited on the glass surface and surrounded by a grid of thin polymer film. One square is unambiguously located by photoetched numbers on this grid. (b) 10×10 μm^2 zoom of the white-light image. (c) Corresponding 10×10 μm^2 AFM scan. (d) Corresponding raster-scan SHG image. Circles in (c) pinpoint the nanoparticles in the AFM image which are SHG-active. Note that a small triangular area in the bottom-left corner is not scanned by the AFM in (c), thus missing one SHG emitter evidenced in (d).

at 986 nm so that the light-matter interaction is highly non-resonant both at this fundamental and the corresponding 493-nm second-harmonic wavelength, where KTP remains highly transparent.(Hansson et al., 2000)

The previously observed domain (see Figures 3b and 3c) is raster scanned and the SHG signal is collected in the backward direction with the same microscope objective and is detected by avalanche photodiodes operated in the photon-counting regime (Figure 3d). SHG is detected from a large fraction of the scatterers revealed by the white-light observation of the sample, as evidenced by the one-to-one correspondence between the spots that appear in Figure 3b and Figure 3d. Nearly all these emitters can also be unambiguously identified in the AFM image (white circles in Figure 3c). The AFM measurement determines the height of the nanocrystals, a value taken as an estimate of the nano-KTP size. A shape and phase analysis of the AFM scan indicates that other non-emitting nano-objects observed in the AFM image are most likely small polymer residues left after the etching process of the polymer during the structuration procedure.

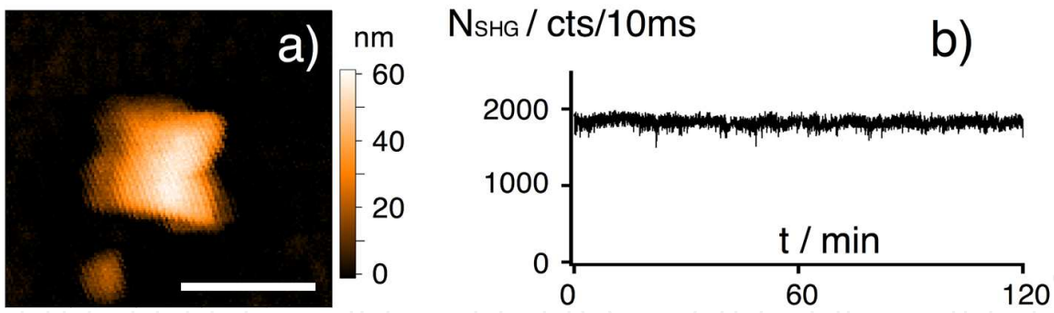

Fig. 4. Characterization of an isolated nano-KTP: (a) AFM image (scale bar: 200 nm), (b) photostability of the second-harmonic emission by the nano-KTP with average incident power 8 mW. Quadratic power dependence of the signal, as expected for SHG, has also been checked (not shown).

We now focus on the study of an isolated nano-KTP, which corresponds to the spot labeled #1 in Figure 3c and 3d. This single particle is representative of the properties of a large number of similar nanocrystallites. A zoom of the AFM image shown in Figure 4a reveals a single particle of almost rectangular shape, with a 60-nm height and a size of 120 nm in its transverse dimensions. We note that the value of the transverse size is over-estimated, due to convolution of the nanocrystal shape with the AFM tip and to residual polymer that might have stuck to the nano-KTP sides. The corresponding SHG image in Figure 3d is a diffraction-limited spot as expected for an emitter with sub-wavelength size. The emitted photon flux at the center of the spot leads to 2.5×10^5 detection counts per second for an average incident power of 8 mW. It leads to a measured signal-to-background ratio as large as 250. Most remarkably, Figure 4b shows the photostability of the emitter under ambient conditions (room temperature and direct exposure to oxygen) since a constant detection signal is recorded for more than 120 minutes. This feature is due to the highly non-resonant character of the interaction: indeed, there is no population in any excited level that could lead to the occurrence of photoinduced degradation processes.

3. Defocused imaging of second harmonic generation from a single nanocrystal

Under similar experimental conditions, we found that the second-harmonic reflection of a strongly focused infrared excitation beam at the surface of a macroscopic KTP crystal with known axis orientation can be accurately modeled by the radiation of a single nonlinearly induced dipole.(Le Xuan et al., 2006) To analyze the second-harmonic emission of a single nano-KTP with sub-wavelength size, we apply the same model which neglects depolarizing and propagation effects associated to the dielectric material.(Bohren & Huffman, 2004) Under an incident electromagnetic field at fundamental frequency ω, the nano-KTP is then equivalent to a single dipole oscillating at frequency 2ω, with components associated to the second-order susceptibility tensor coefficients

$$P_i^{2\omega} = \epsilon_0 \sum_{j,k} \chi_{ijk}^{(2)}(-2\omega;\omega,\omega) E_j^{\omega} E_k^{\omega} \tag{1}$$

where i, j, k span the Cartesian coordinates x, y, z in the laboratory frame. Describing the orientation of the crystal axes by the Euler angles , the nonlinear coefficients in the labora-

tory frame are related to the known nonlinear coefficients in its crystallographic X, Y, Z axes through simple rotations

$$\chi^{(2)}_{ijk} = \sum_{J,K} \chi^{(2)}_{IJK} \cos(\vec{i},\vec{I}) \cos(\vec{j},\vec{J}) \cos(\vec{k},\vec{K}) \quad (2)$$

The resulting nonlinear dipole radiates a second-harmonic field , which is predicted to have a specific polarization through equations 1 and 2. Following recently developed polarimetry techniques for nonlinear microscopy,(Brasselet et al., 2004; Le Floc'h et al., 2003) a polarizing beamsplitter analyzes the SHG orthogonal field components along x and y laboratory axes, located in the plane perpendicular to the microscope optical axis z. Each corresponding intensity is recorded as the excitation field is rotated with a half-wave plate in the path of the incident beam. Qualitatively, the polar graph of Figure 5a displays x and y second-harmonic emission similar to dipolar radiative patterns. They are related to the projection of the nonlinear emitting dipole in the (x,y) plane, i.e. Euler angle ϕ. In the case of a single nonlinear coefficient being non-null in Equations 1 and 2, we would have obtained two homothetic polar graphs. The different responses along x and y are due to the contribution of the five nonlinear coefficients in the KTP tensor.(Sutherland, 1996) Here, equations 1 and 2 allow us to retrieve $\phi = 70^\circ \pm 5^\circ$.

This polarimetry technique has however a low sensitivity to any dipole component along the longitudinal z-axis. To retrieve the orientation of the dipole in the three dimensions, we apply a defocused imaging technique.(Bohmer & Enderlein, 2003; Brokmann et al., 2005; Sandeau et al., 2007) For a given direction of propagation in the far field, the radiated field is proportional to

$$\vec{E}^{2\omega}_{FF} \propto \vec{k} \times \vec{k} \times \vec{P}^{2\omega} \quad (3)$$

while the intensity radiation diagram is given by, $I^{2\omega}_i(\vec{k}) \propto |\vec{E}^{2\omega}_{i,FF}(\vec{k})|^2$, where i stands for x, y, z. This radiation diagram is directly measured as a function of excitation polarization orientation by positioning a highly-sensitive CCD camera slightly out of the conjugated focal observation plane. The experimental defocused image is displayed in Figure 5b. Qualitatively, the outer "moon-shaped" structure is characteristic of an emitting dipole out of the (x,y) plane of the sample.(Bohmer & Enderlein, 2003; Brokmann et al., 2005; Sandeau et al., 2007) Compared to the case of single-chromophore fluorescence,(Bohmer & Enderlein, 2003; Brokmann et al., 2005) the image exhibits specific features associated to the nonlinear coupling described by equation 1 between the nonlinearly induced dipole and the polarization state of the excitation field . This allows us to determine the full set of Euler angles of the observed nanocrystal with a good accuracy while relying only on the SHG signal.(Sandeau et al., 2007) For the chosen nano-KTP #1 of Figure 3c, the model developed in (Sandeau et al., 2007) gives a single set of angles: Figures 5c and 5d display the numerical simulations corresponding respectively to Figures 5a and 5b with the determined Euler angles of the crystal axes.

For more insight on the method, we focus in the next part on a more detailed 3D orientation determination of one typical single KTP nanocrystal. The experimental setup is described in Figure 2. For defocused imaging, the SHG signal is directed towards a sensitive CCD camera (CCD_2 on the setup figure, having 512×512 pixels, 13×13 μm^2 pixel size, thermoelectrically cooled) which is translated by 15 mm towards the objective, so as to obtain a contrasted image of about 600×600 μm^2 size.

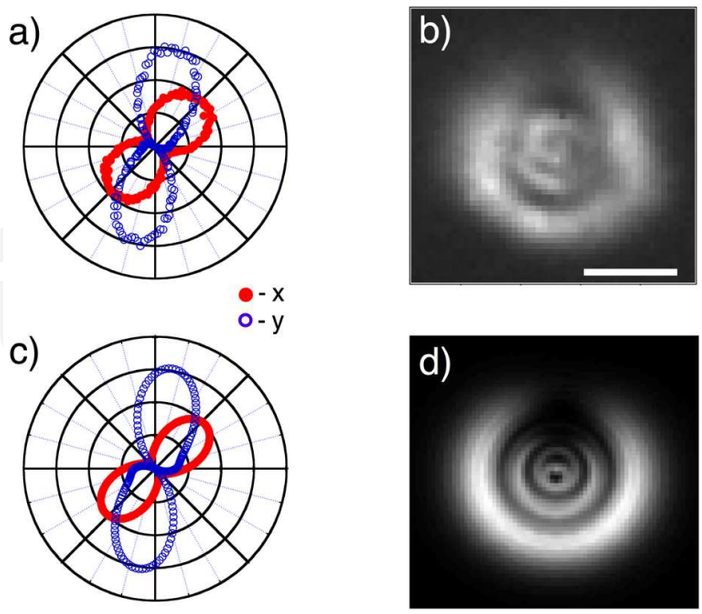

Fig. 5. 3D orientation of an isolated nano-KTP: (a) polar graph showing the measured SHG emission of the nanocrystal along x (red points) and y (blue points) axes, as a function of the direction of the linearly polarized excitation field, (b) corresponding experimental defocused image (scale bar: 250 μm), (c) and (d) numerical calculation of the polar graph and the defocused image respectively for a nano-KTP with Euler angles of the crystalline axis equal to ($70^\circ \pm 5^\circ$, $15^\circ \pm 5^\circ$, $60^\circ \pm 5^\circ$).

Figure 6 exhibits measured defocused images from a single KTP nanocrystal for different polarization orientations of the incoming fundamental field in the sample plane. Different features appear on these images. First, they exhibit a symmetry axis which orientation in the sample plane is related to the nanocrystal in-plane orientation. Second, the structure of the image is characteristic of a nanocrystal exhibiting out-of-plane orientation with $\theta \neq 0^\circ$. Third, the symmetry axis of the structure rotates when changing the incident polarization direction. This is characteristic from a nonlinear coherently induced dipole emission as opposed to a single fluorescent dipole, since the KTP multipolar symmetry structure allows coherent nonlinear coupling with various incident field polarization directions.
The measured images are interpreted using a vectorial model calculation, in which the KTP nanocrystal is modeled by a cubic shape sampled by placing one individual dipole every nm^3 within this cube. The experimental imaging configuration is taken into account. Starting from the ring pattern observation for a first estimate of the 3D orientation parameter, the emission pattern calculation (Fig. 6(f-j)) is then implemented to manually adjust at best the measured images (Fig. 6(a-e)). This leads to a 3D orientation determination with error margins of $\pm$ 5° at maximum for θ and ϕ. This error is much larger for the ψ Euler angle (from $\pm$ 10° to $\pm$ 50°), which is specific to the case of KTP for which there is only a weak difference between nonlinear coefficients involving the "1" and "2" directions perpendicular to the main "3" axis.(Vanherzeele & Bierlein, 1992) In order to confirm the values for the obtained orientation angles, they were used as input parameters to calculate the in-plane polarimetric SHG response of the measured nanocrystal. The corresponding angular dependencies agree well

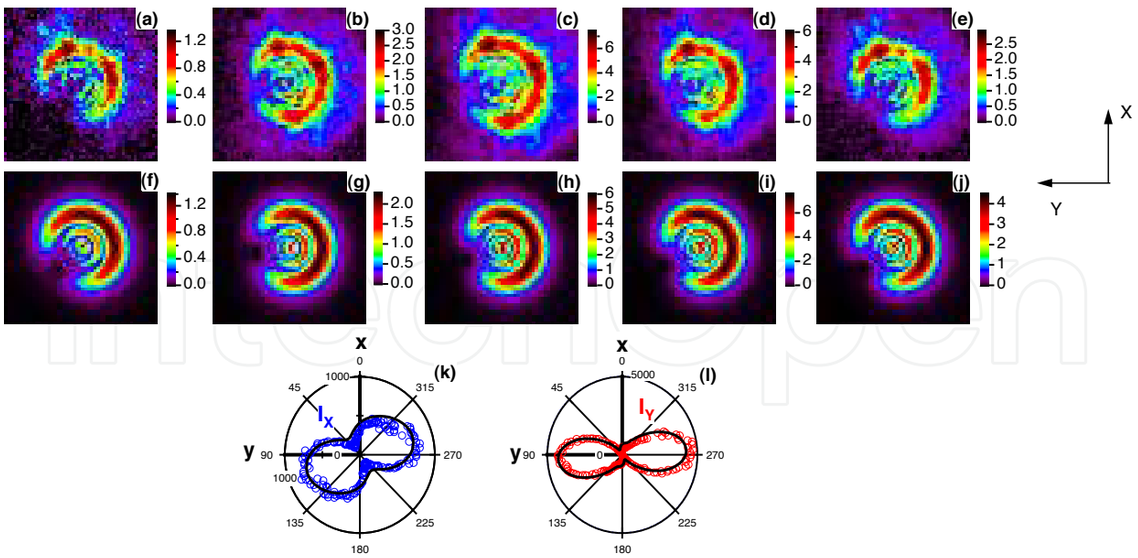

Fig. 6. (a-e) Experimental defocused images of a KTP nanocrystal for several incident polarization directions relative to the x-axis: (a) 0°, (b) 60°, (c) 90°, (d) 120° and (e) 150°. The images sizes are 600×600 μm^2. The integration time for each image is 5 s. (f-j) Corresponding calculated images, leading to the orientation parameters $(\theta = 30° \pm 5°, \phi = 115° \pm 5°, \psi = 90° \pm 20°)$. (k,l) Experimental polarimetric analysis Ix and Iy of this nanocrystal (circle markers) and corresponding calculated polarization responses (lines) for the Euler set of angles deduced from the defocused imaging analysis.

with the experimental data (Fig. 6(k,l)). Note that a direct determination of the Euler angles from such polarimetric responses would have been more delicate since the KTP symmetry exhibits several ambiguous situations when projected in the sample plane. This points out the advantages of the defocused imaging technique, which encompasses a complete 3D coupling information in the observed pattern shapes.

Performing numerical simulation on nanocrystal of different sizes, we note that that small differences occur but in general the patterns of the defocused images have similar features, with a symmetry axis along the direction of the nonlinear induced dipole. The ring-structured shape appears to be in all cases representative of the tilt angle of the "3" axis of the crystal with respect to microscope objective axis z. The rough similarity among the observed pattern with respect to crystal size shows that radiation imaging can be used as a robust technique to determine orientation independently on the crystal size, provided that it lies below 150-200 nm. Above this size range, the fine structure of the observed rings is seen to clearly deviate from the single dipole model. For KTP nanocrystal of size smaller than 100 nm in diameter, the SHG emission can be modeled correctly in a dipolar approximation. In addition to 3D orientation determination, such a technique presents the unique property of providing a diagnostics for the crystalline quality of an isolated nano-object. Indeed the presence of nanocrystals of different orientations in a same focus point would strongly affect the defocused image properties described above, and allow a direct conclusion on the mono-crystallinity of the observed object. This is illustrated in Fig. 7, representative of a nanometric size KTP for which images are deprived from a symmetry axis and deviate from the previously observed ring structures. Such images are representative of the presence of at least two KTP nanocrystals in the focal

volume of the microscope objective, which could not be revealed by the sole observation of the diffraction-limited spot size.

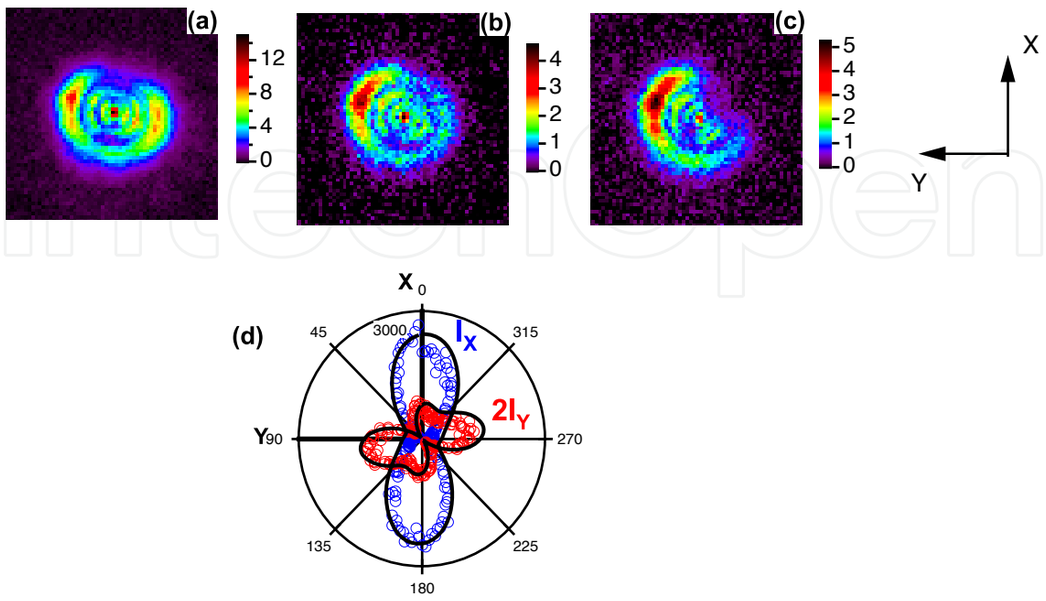

Fig. 7. (a-c) Defocused images of a nanocrystal for several incident polarization directions relative to the x (horizontal) axis: (a) 0°, (b) 306° and (c) 90°. The images sizes are 800×800 μm^2. This nano-object is visibly constituted of several distinct sub-domains, (d) Polarimetric analysis of this nano-cluster of nanocrystals. The adjustment of polarimetric responses (black line) is done using two nanocrystals of respective orientations $(\theta_1 = 20°, \phi_1 = 260°, \psi_1 = 0°)$ and $(\theta_2 = 45°, \phi_2 = 350°, \psi_2 = 0°)$.

A finer observation allows us to conclude that in this two-KTP nanocrystals picture, one of them is likely to lie close to the vertical x axis of the images, since the SHG pattern approaches a ring structure for a x-polarized excitation. The other KTP nanoparticle is preferentially excited for a polarization angle close to 45° (relative to x), and therefore manifests with larger signals in Fig. 7(b,c) as the excitation angle increases. This deviation from a mono-crystalline structure is confirmed in the polarimetric response of such a nano-object, which curve cannot be fitted using a single KTP unit-cell model, but rather by two or more nanocrystals orientations.

We have demonstrated in this section that defocused imaging of second harmonic generation radiation from a single KTP nanocrystal can provide a direct retrieval of its 3D orientation. This orientation information, based on the knowledge of the nano-object crystalline symmetry, can thus be used as a complete characterization of the excitation-dependent polarization state from a nonlinear nanosource. In addition, we show that this technique provides a unique possibility to inform on the mono-crystallinity nature of a nano-object. Finally, this analysis method is a promising tool of analysis of the vectorial electric-field character from an unknown electromagnetic incident radiation, taking advantage of the rich features appearing from the nonlinear coupling between matter at the subwavelength scale and complex optical polarization components.

4. Balanced homodyne detection of second harmonic radiation from single KTP nanocrystal

SHG is a coherent process thus interferometric detection schemes are well suited to the detection of the emitted field. Among possible techniques, coherent balanced homodyne is known to exhibits a sensitivity to extremely low photon flux rates (Yuen et al., 1983). Although high sensitivity with such a technique has been demonstrated to detect surface SHG emission from an air-semiconductor interface (Chen et al., 1998), to the best of our knowledge it had never been applied to the study of nano-objects. Since the optical phase of the SHG emitted field is directly related to the sign of the associated nonlinear susceptibility, measuring directly its value provides important information about the nonlinear material (Stolle et al., 1996). At nanometric scale, it allows to determine the absolute orientation of dipoles with nonlinear hyperpolarisabilities such as organic nanocrystals (Brasselet et al., 2004), to detect the polarity in cell membranes (Moreaux et al., 2000), or to study the boundary between microscopic crystalline domains (Laurell et al., 1992). Such application prospects strongly motivate the development of phase-sensitive SHG microscopy with highly sensitive detection compared to SHG interferometric schemes previously developed (Stolle et al., 1996). In this work coherent balanced homodyne detection is associated to SHG microscopy, allowing us to detect nano-objects with high signal-to-noise ratio and phase sensitivity.

The principle of the experiment is shown in Fig.8. Femtosecond infrared light pulses are injected in an inverted optical microscope and tightly focused. Backward second-harmonic emission by a nonlinear crystal placed on a glass cover slide at the microscope focus is collected by the microscope objective and transmitted through a dichroic mirror toward the detection set-up. A small fraction of the fundamental beam is also reflected from the cover-slide and follows the same optical path, providing the phase reference. Second-harmonic emission of the crystal, further referred as "signal", corresponds to an electrical field $E^{(2\omega)} = |E^{(2\omega)}| \exp[i\,\Phi_{\text{obj}}^{(2\omega)}]$, where $\Phi_{\text{obj}}^{(2\omega)}$ is the phase shift of the SHG field emitted by the object as compared to the one of the incident fundamental field $E_{\text{in}}^{(\omega)}$ on the object. For a macroscopic nonlinear crystal, the SHG field is $E^{(2\omega)} \propto \chi^{(2)} {E_{\text{in}}^{(\omega)}}^2$. Thus, $\Phi_{\text{obj}}^{(2\omega)}$ reflects the phase of the nonlinear susceptibility $\chi^{(2)}$. For a nonlinear crystal in its spectral transparence window, $\chi^{(2)}$ is real with a positive or negative value depending on the absolute orientation of the nonlinear response in respect to the crystal axis. Therefore determination of $\Phi_{\text{obj}}^{(2\omega)}$ allows to infer the absolute orientation of the nonlinear crystal.

For the coherent optical homodyne detection of the SHG signal, the local oscillator (LO) is generated by sending part of the incident infrared beam into a bulk BBO nonlinear crystal (Fig.8). A Glan prism ensures linear polarization of the local oscillator along the x-axis and x-polarized signal and local oscillator are recombined by a non-polarizing 50/50 beamsplitter cube. The 180° out-of-phase interferences at the two output ports of the beamsplitter are detected by photodetectors D_1 and D_2. In balanced detection mode, the two resulting photoelectric signals S_1 and S_2 are subtracted [1], thus canceling out their DC component. The interferometric signal is then

$$\Delta S^{(2\omega)} = K \times 2V \sqrt{P_{\text{LO}}^{(2\omega)} P_{\text{sig}}^{(2\omega)}} \cos\left(\Phi_{\text{sig}}^{(2\omega)} - \Phi_{\text{LO}}^{(2\omega)}\right) \tag{4}$$

[1] We use an autobalanced photoreceiver (Nirvana, Model 2007, New Focus, San Jose CA) which achieves 50 dB common noise rejection

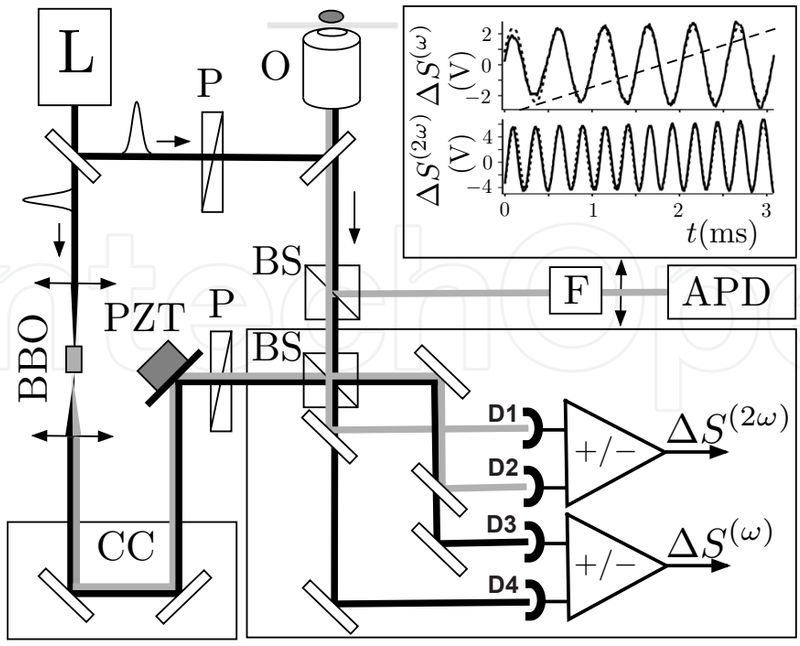

Fig. 8. Schematic of the experimental set-up. L: femtosecond laser (86 MHz repetition rate, $\approx$ 100 fs pulse duration, $\lambda = 986$ nm); BBO: nonlinear $\chi^{(2)}$ crystal; P: Glan prism; O: microscope objective (N.A. = 1.40, $\times$ 100) leading to a $\approx$ 300 nm FWHM diameter focal spot; BS: non-polarizing beamsplitter; CC: corner-cube; PZT: mirror mounted on a piezoelectric transducer; KTP: macroscopic $KTiOPO_4$ crystal or single sub-wavelength size crystal; F: SHG filter; APD: avalanche photodiode in photon counting regime; D_1 and D_2: p-i-n Si photodetectors of the balanced receiver recording SHG at 2ω (a SHG filter, not shown, is put in front of the detectors); D_3 and D_4: the same for the balanced receiver at fundamental optical frequency ω (an IR filter, not shown, is put in front of the detectors). *Insert*: full lines : detected signals as a function of time for a forward translation of the mirror. Up: signal $\Delta S^{(\omega)}$ at fundamental frequency with a sinusoidal fit at frequency $f = 1.9$ kHz, and bottom: $\Delta S^{(2\omega)}$ at SHG frequency with a sinusoidal fit at frequency $2f$ = 3.8 kHz, dashed line: voltage applied to the PZT on half a period (vertical scale: a.u.).

where $P_{\mathrm{LO}}^{(2\omega)}$ and $P_{\mathrm{sig}}^{(2\omega)}$ denote the mean optical power of local oscillator and signal, V is the fringe visibility, and K includes the quantum efficiency of the photodiodes. The phase shift of the signal at frequency 2ω , $\Phi_{\mathrm{sig}}^{(2\omega)} = \Phi_1^{(2\omega)} + \Phi_2^{(2\omega)}$ contains the phase shift $\Phi_1^{(2\omega)}$ of the x-polarized radiation emitted by the nonlinear object and the phase shift $\Phi_2^{(2\omega)}$ due to propagation in the interferometer.

In order to measure the phase shift $\Phi_{\mathrm{sig}}^{(2\omega)}$, temporal interference fringes are created by displacing a mirror mounted on a piezoelectric transducer (PZT) driven with a triangular shape voltage. The resulting fringes are shown in the inset of Fig.8. To extract the phase shift information, fringes at 2ω are compared to reference fringes resulting from fundamental beam. More precisely, we perform with detectors D_3 and D_4 a separate balanced homodyne detection of the residual fundamental beam reflected by the sample by mixing it with the residual light at ω

which follows the reference arm. A reference interference signal (see inset of Fig. 8) is then obtained, equal to $\Delta S^{(\omega)} = K' \times 2V' \sqrt{P_{\mathrm{LO}}^{(\omega)} P_{\mathrm{sig}}^{(\omega)}} \cos\left(\Phi_{\mathrm{sig}}^{(\omega)} - \Phi_{\mathrm{LO}}^{(\omega)}\right)$ with same notations meaning as in Eq. 4. The quantity to be extracted is then $\Delta\Phi = \left(\Phi_{\mathrm{sig}}^{(2\omega)} - \Phi_{\mathrm{LO}}^{(2\omega)}\right) - \left(\Phi_{\mathrm{sig}}^{(\omega)} - \Phi_{\mathrm{LO}}^{(\omega)}\right)$ which can be written as $\Delta\Phi = \Phi_1^{(2\omega)} + \Phi_0$, where Φ_0 is an "instrumental" phase shift. Although Φ_0 can be measured with a reference crystal its value is not required if we are only concerned in variation of $\Phi_1^{(2\omega)}$ while keeping Φ_0 constant. Finally, the value of $\Delta\Phi$ is extracted using a numerical procedure.

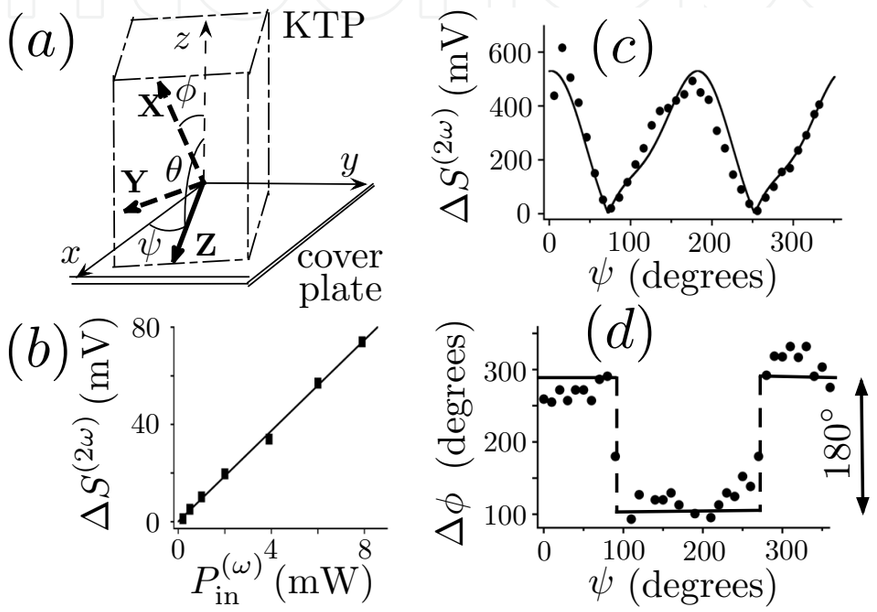

Fig. 9. Results from the balanced homodyne detection. (a) Laboratory axes (x, y, z) with x-polarized incident fundamental beam propagating along z-axis. (**X**, **Y**, **Z**) KTP crystal principal axes ($\theta = 90°$ and $\phi = 23.5°$). Full lines denote axes in the (x, y) plane. ψ : rotation angle of the $\chi^{(2)}$ nonlinear crystal around the z-axis. (b) Linearity of $\Delta S^{(2\omega)}$ as a function of fundamental incident power. Points : experimental data, full line : best linear dependence fit. (c) : $\Delta S^{(2\omega)}$ as a function of ψ (in degrees). (d) : Relative SHG phase shift $\Delta\Phi$ as a function of ψ.

A bulk KTP crystal with axes as shown in Fig.9 is used to test the setup. The Z-axis is parallel to the crystal input face. With a strongly focused pump beam, a SHG backward emitted beam from the interface is observed (Boyd, 2003). We first check in Fig.9b that $\Delta S^{(2\omega)}$ associated to this surface SHG grows linearly with the fundamental incident power on the crystal $P_{\mathrm{in}}^{(\omega)}$, as expected from Eq.4. If the crystal is rotated by 180° around the microscope optical axis (z-axis), the nonlinear coefficient $\chi^{(2)}$ is transformed in $-\chi^{(2)}$ and a 180° SHG-phase-shift is expected. Results are shown in Fig.9c. The amplitude shows a maximum of x-polarized SHG when the linear polarization is aligned along the Z-axis of the crystal (ψ = 0° or 180°) which exhibits the highest nonlinear coefficient. The full line is the theoretical result assuming an x-polarized incident plane wave normal to the interface and a single nonlinear emitting dipole which takes into account all nonlinear coefficients of the KTP $\chi^{(2)}$ tensor. It yields good agreement

with experimental points. The phase-shift $\Delta\Phi$ (Fig. 9d) remains constant while the nonlinear dipole has a positive projection along the x-axis ($0° < \psi < 90°$). It then endures a 180ą-phase-shift when it becomes negative ($90° < \psi < 180°$). The small deviation to the constant value is attributed to drift of the ϕ_0 parameter during the step-by-step rotation of the KTP crystal.

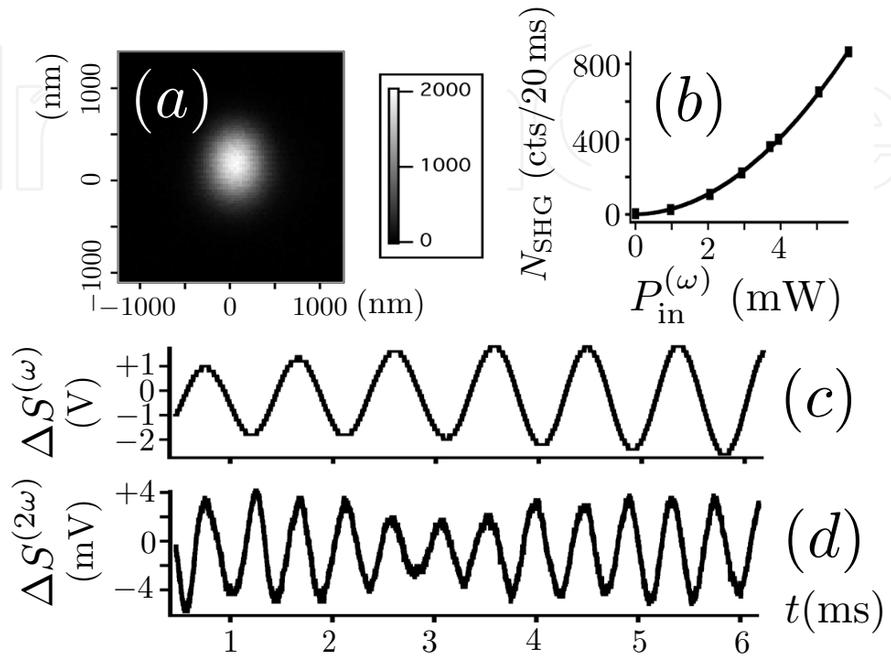

Fig. 10. Application of the balanced homodyne technique to sub-wavelength-size nonlinear crystals. (a) Raster-scan image of SHG signal from a KTP nano-crystal with an avalanche photodiode. The FWHM diameter of SHG spot intensity is about 300 nm, very close to the theoretical two-photon microscope resolution (320 nm FWHM). (b) Number of detected SHG photons as a function of incident power with a best square-law dependence fit. (c) Fundamental interference signal $\Delta S^{(\omega)}$ as a function of time for a single nano-crystal and (d) corresponding SHG interference signal $\Delta S^{(2\omega)}$.

We then apply the method to the detection of SHG from KTP nanocrystals. To first locate the crystals, the sample is raster-scanned in x and y directions with piezoelectric translators and SHG is detected with the avalanche photodiode as shown in Fig.10. A SHG signal image of such a nano-crystal is shown in Fig.10a. A quadratic dependence of the detected SHG intensity is observed upon varying $P_{\mathrm{in}}^{(\omega)}$ as expected (see Fig.10b). After positioning the focused infrared excitation beam at the center of the detected emission spot of a single nano-crystal, we switch to the coherent balanced homodyne detection set-up. SHG interference fringes (Fig.10d) associated to fundamental ones (Fig.10c) are clearly visible, giving evidence for the coherence of the nano-crystal SHG emission.

Since the balanced homodyne detection method consists in the projection of the signal electric field on the spatio-temporal mode of the local oscillator, mode-matching between signal and LO beams determines maximal amplitude of the fringes. This can be quantified by the fringe visibility V of Eq.4 being equal to unity for perfect mode-matching. With a 2 mW LO average

power, the smallest SHG fringe amplitude measured with 1 s duration averaging is equivalent to a signal power $P_{\text{sig}}^{(2\omega)} \approx (7.2 \pm 5.0) \times 10^{-19}$ W assuming $V = 1$. The uncertainty evaluated for 95 % confidence interval is equivalent to 3.2 detected photons/s, close to the shot noise limit. However a unity fringe visibility is practically difficult to achieve. In an auxiliary experiment using equal powers for signal and LO beams, we measure $V = 0.21$, leading to an actual sensitivity of 80 photons/s. Such a reduced value for the visibility factor is attributed to imperfect mode-matching between signal and LO modes, including polarization mismatch, wave-front distortion, and frequency chirp on the SHG-emitted femtosecond pulses.
To conclude this section, we have demonstrated a SHG phase-sensitive microscope with coherent balanced homodyne detection, showing a sensitivity at the photon/s level. The high-spatial resolution and the sensitivity of the technique is well-adapted to the study of SHG from nano-crystals.

5. Coherent nonlinear emission from a single KTP nanoparticle with broadband femtosecond pulses

As a coherent process, the number of SHG photons emitted by a noncentrosymmetric nanoparticle scales as the square of the number of "oscillators" in the nanocrystal, i.e., as the sixth power of the nanoparticle average size. As a two-photon process the SHG intensity is also expected to scale, for a constant average laser power, as the inverse of the pulse time duration. It is therefore tempting to reduce the pulse duration from the standard 100 fs to 10 fs available from broadband ultrafast lasers in order to enhance the second harmonic photon emission rate by an order of magnitude, thus reducing the limit size of detectable nanoparticles. Nevertheless, this downscaling has to be done with care since high-order phase dispersion of the microscope objective and other optical components induce temporal aberrations in the excitation pulse interacting with the nanoparticle at the focus of the microscope (Guild et al., 1997). Using recently developed techniques for temporal characterization at the microscope focus and careful precompensation (Lozovoy et al., 2004), SHG from large objects has indeed been shown to scale as the inverse of the pulse time duration (Xi et al., 2008). Additionally, the broadband excitation corresponding to a 10-fs pulse offers the possibility of spectral manipulation for coherent control (Warren et al., 1993; Weiner, 2000) of two-photon absorption and non-resonant second harmonic generation (Broers et al., 1992; Meshulach & Silberberg, 1998; Wnuk & Radzewicz, 2007).
While it has been recently shown that a SHG-active nanoparticle of a size about a few hundreds of nanometers can be used for pulse detection in a nanoscopic version of the FROG technique (Extermann et al., 2008), the effects of manipulation of the excitation beam on SHG emission, i.e.,decreasing the time duration of a precompensated pulse as well as structuring its broadband spectrum, have not yet been investigated at the single nanoparticle level with a size well below the wavelength of light. Moreover in this size range phase matching conditions are automatically fulfilled, improving the coherent emission. Here we have shown that the use of broadband ultrashort laser pulses, precompensated using an automatic genetic algorithm,improves the second harmonic emission from a single nanoparticle of size about 100 nm. It results in a contrast enhancement of the SHG image obtained by raster scanning the sample. In this process, smaller nanoparticles are revealed for a given background. We also manipulate the broadband incident spectrum in a very simple manner to obtain a non-degenerate sum-frequency generation from a single nanoparticle.

The experiment is realized using a titanium doped sapphire (Ti:Sa) femtosecond laser with a 100 nm bandwidth. The laser spectrum is sufficiently broad to support pulses of approximately 10 fs duration. A genetic algorithm (Baumert et al., 1997) is used to search for the best phase correction on the incident pulse. A bulk KTP crystal with one face polished served as reference sample. Under femtosecond beam illumination, the second harmonic signal emitted by the crystal and detected with an avalanche photodiode operated in photoncounting regime served as the feedback information in the genetic algorithm procedure. The bulk crystal, instead of a nanocrystal, was selected because it provides a high signal to noise ratio, which speeds up the search for the optimal phase of the excitation pulse.
The phase correction was achieved with two consecutive systems: a two-prism compressor used for the rough compensation of (mostly quadratic) phase, and a compact pulse shaper using a diffraction grating and a spatial light modulator (SLM) (Weiner, 2000). The SLM-based pulseshaper was used for the genetic algorithm search for the optimal phase. To evaluate the result of this search we estimated the duration of the excitation pulse at the focus of the microscope by recording the interferometric autocorrelation of the pulse using the second harmonic field generated in the KTP nonlinear crystal. The result of the genetic algorithm search leads to a pulse of, approximately, 13 fs duration. Once the optimal pulse shape was found its duration can then be increased to any value by adding, with the SLM, a controlled amount of the second-order phase. The corresponding SHG photon number was then measured as a function of the corresponding pulse duration.

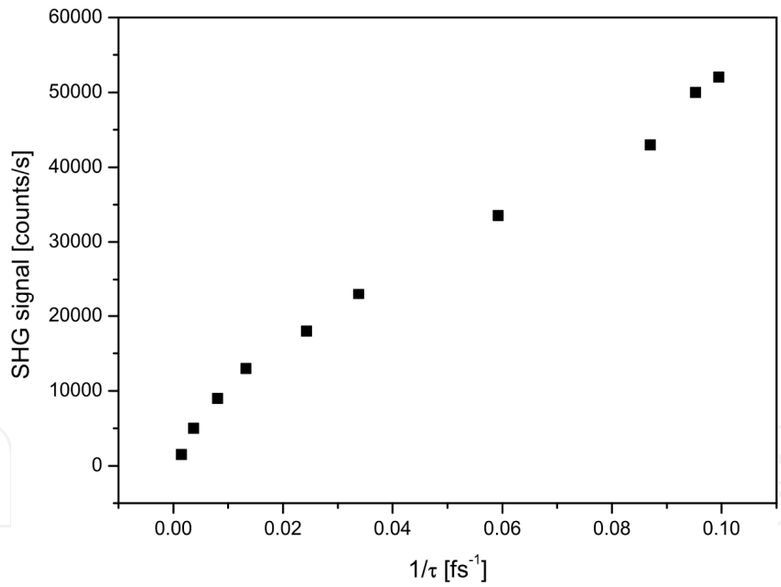

Fig. 11. Detected rate of the SHG from a 100 nm KTP nanocrystal as a function of pulse time duration showing the improvement of the SHG signal with the inverse of the pulse duration.

For a constant average incident power, the SHG signal is expected to scale as the inverse of the duration of the pulse at the microscope focus. Indeed, we observed a linear increase of the SHG signal with the inverse of the time duration, as shown in Fig. 11. However, the measured average slope is approximately 0.7 instead of unity. This is due in part to the broadband spectrum which cannot be perfectly compressed by the SLM due to pixelization of the correction signal and imperfections in spectral wings compensation. Analysis of the data shown

in Fig. 11 reveals that the slope is indeed close to unity for long pulses, while it decreases with the pulse duration. Such a behavior is consistent with imperfect phase compensation: even small phase errors become important when the pulse duration approaches the Fourier transform limit. Despite this imperfect phase compensation, the SH count rate is nevertheless improved by almost an order of magnitude, as compared to excitation by standard 100 fs pulses with the same average intensity. With precompensated pulses, we recorded raster-scan maps of the SH signal originating from well dispersed KTP nanoparticles deposited by spin-coating a colloidal solution on a glass cover-slip. Figure 12 shows maps of the same area of the sample recorded with different pulse durations ranging between 200 fs and 13 fs. Firstly, for nanoparticles already visible at 200 fs, a clear increase of the signal-to-noise ratio is observed for shorter pulses. Secondly, Fig.12 reveals that a higher number of nanoparticles appear in the maps acquired with shorter pulses, since smaller objects can be detected due to enhanced second harmonic emission. This contrast enhancement is crucial for many practical applications of nonlinear microscopy.

The pulse autocorrelation measured on an individual KTP nanocrystallite in the focus of the microscope is close to the Fourier limit, which confirms the efficiency of the phase compensation and gives evidence that all spectral components of the precompensated pulse are converted by the nanoparticle. We note that the bandwidth of the SHG is, for bulk nonlinear crystal, limited by phase matching conditions (Boyd, 2003). However, because of the sub-wavelength dimension of the nanoparticle spectral filtering associated to phase-matching becomes negligible even for ultrashort femtosecond laser pulse.

The broadband nonlinear response opens the way to the coherent control of the different spectral components of the single incident beam in order to manipulate the second-order nonlinear emission (Dudovich et al., 2002).

As a proof-of-principle of such spectral manipulation, we used a two-band incident spectrum, containing well-separated but coherent "red" and "blue" parts (see inset of Fig. 13),in order to excite and subsequently filter out a non-degenerate sum-frequency (SF) signal. If we simply assume two average excitation frequencies "R" and "B" in the single incident beam,the SF signal is due to a nonlinear polarization of the form (Boyd, 2003):

$$P^{\omega_R+\omega_B} = \epsilon_0 \sum_{j,k} \chi^{(2)}_{ijk}(-\omega_R - \omega_B; \omega_R, \omega_B) E_j^{\omega_R} E_k^{\omega_B} \tag{5}$$

where i, j, k stand for x, y, z, the laboratory axes. With two well-separated spectral bands, Eq.5 shows that we have access to the different polarizations j, k of the driving fields, then select a specific nonlinear coefficient $\chi^{(2)}_{ijk}$, and thus control the direction i of the nonlinear dipole at the generated sum frequency. This can be applied e.g. to enhance the recognition of the nanoparticle-marker in a complex environment, and to investigate the shape dependence of the nonlinear optical response of an individual nanoparticle. Yet another possible future application concerns the measurement of the polarization properties of a femtosecond pulse in the focus of a microscope objective. In principle, the spatial resolution of such a measurement is limited by the minimum size of the nanocrystallite that produces a measurable signal. With sub 100-nm detection limit demonstrated in our experiment we hope to obtain in the future a detailed 3-D map of the polarization in the vicinity of the focus.

A simple two-band excitation is performed, as an experimental proof of principle, by blocking a part of the incident pulse spectrum. A bandpass filter is then placed in the detection path to transmit $\omega_R + \omega_B$, and reject both $2\omega_R$ and $2\omega_B$. We checked that excitation with any single spectral band, i.e., ω_R or ω_B, does not produce SF signal. Varying the power of the blue band

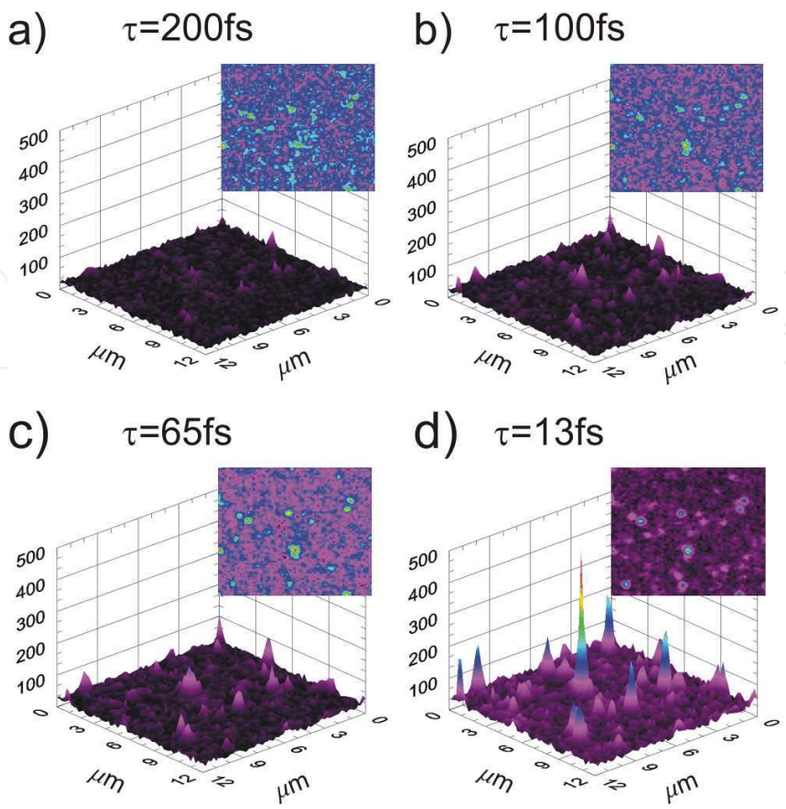

Fig. 12. SHG maps of the same area of the nanoKTP sample. The maps correspond to excitation with pulse durations of (a) 200 fs (SNR=2.5), (b) 100 fs (SNR=4), (c) 65 fs (SNR=4.5) and(d) 13 fs (SNR=16). For each pulse duration both a three-dimensional graph of the SH intensity as well as a normalized two-dimensional map are shown.

of the spectrum while keeping fixed the intensity of the red band leads to a linear increase of SFG vs. blue band power (Fig. 13), as expected from Eq. 5. Due to the intrinsic absence of ensemble averaging, this result can be considered as an improved version of Kurtz powder method (Kurtz & Perry, 1968), now applied on a single 100-nm size nonlinear nanoparticle.
To conclude this section, we have shown that phase-compensated 13-fs infrared pulses generated through the application of a genetic algorithm allow one to gain about one order of magnitude (as compared to standard 100-fs pulses with the same average intensity) in the SHG emission rate of a non-centrosymmetric single KTP nanocrystal. This leads to efficient optical detection of smaller nanocrystals which appear only when shorter pulses are used. Since there is no phase-matching limitation on the bandwidth of the excitation pulses, even shorter (sub-10 fs) pulse scan can be used to even further enhance the second harmonic signal. Optical autocorrelation from a nanocrystal with an AFM measured size of about 100 nm has been recorded, showing that pulse characterization can be obtained even on SHG-active nanoparticles of sub-wavelength size.

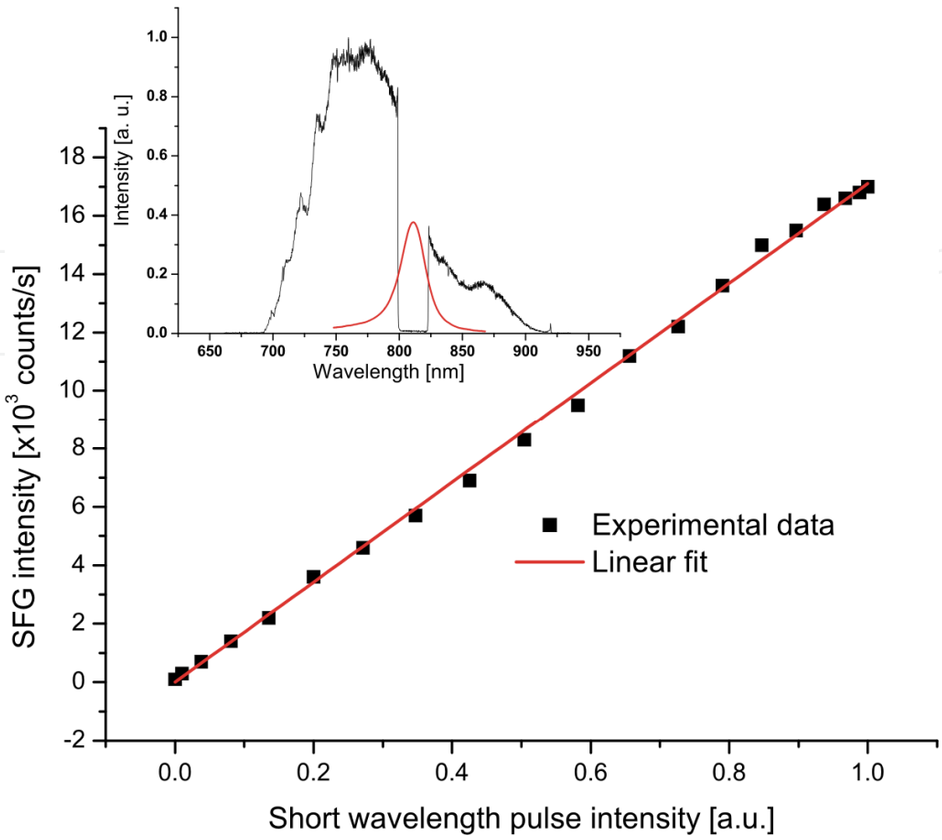

Fig. 13. Coherent sum frequency generation from a single nano-KTP vs the intensity of the blue band. Inset: corresponding pulse spectrum with two distinctive parts "red" and "blue". The nonlinear response is detected in the sum-frequency band with an interference filter transmission (spectral transmission shown in red). Note that in the latter case the wavelength scale has been multiplied by two.

6. Conclusion

In summary, we have reported the observation and the characterization of nanometric-sized crystals extracted by centrifugation from KTP powder. For a well-isolated single nanocrystal, in situ AFM analysis of its size and analysis of its second-harmonic emission properties have been performed. The highly efficient nonlinear response leads to the emission of a large number of SHG photons in a photostable and blinking-free manner due to non-resonant coherent interaction. By recovering the radiation pattern from the recorded defocused images, we retrieve the in situ three-dimensional crystal orientation. Solution-based chemical synthesis of KTP nanocrystals with a monodisperse size controlled by capping agents,(Biswas et al., 2007) now under way, should lead to optimized KTP nanocrystallites and to a more accurate estimate of the size-detection threshold. It also opens the way to surface functionalization of these nanocrystals. Fully characterized nano-KTPs are attractive for the development of novel schemes of nonlinear microscopy. Moreover, due to the non-resonant interaction, they can be envisioned for probing the localized electromagnetic field enhancement that appears at the apex of a metallic tip(Bouhelier et al., 2003) or is randomly generated by granular metallic

structures(Stockman et al., 2004) while avoiding any detrimental quenching effect(Buchler et al., 2005; Carminati et al., 2006) induced by the metallic interface. The coherent character of the second harmonic emission from a single KTP nanocrystal have also been demonstrated in a balanced homodyne detection scheme, which permit nanoparticle detection with high signal-to-noise ratio and phase sensitivity. Furthermore, broadband femtosecond pulses have been successfully employed for studying of a single KTP nanoparticle, which open a bright perpective for spectral manipulation for coherent control of the nonlinear process at the nanoscale.

Acknowledgements

The authors are grateful to Dominique Lupinski and Philippe Villeval from Cristal Laser for initial nanoKTP material, Thierry Gacoin, Sandrine Perruchas, Cédric Tard and Géraldine Dantelle for the fabrication of the nanocrystal solution, Joseph Lautru for sample preparation. We acknowledge Jean-Pierre Madrange, André Clouqueur for technical assistance. This work is a fruitful collaboration with Nicolas Sandeau, Sophie Brasselet, Véronique Le Floc'h, Joseph Zyss, Chunyuan Zhou, Yannick de Wilde, Yannick Dumeige, François Treussart, François Marquier, Jean-Jacques Greffet, Rémi Carminati. This work is supported by AC Nanosience research program, CNano IdF research.

7. References

T. Baumert, T. Brixner, V. Seyfried, M. Strehle, and G. Gerber, "Femtosecond pulse shaping by an evolutionary algorithm with feedback," Appl. Phys. B 65, 779-782 (1997).

S. K. Biswas, A. Pathak, P. Pramanik, "Synthesis of Nanocrystalline $KTiOPO_4$ Powder by Chemical Method" J. Am. Ceram. Soc. 90, 1071 (2007)

M. Bohmer, J. Enderlein, "Orientation imaging of single molecules by wide-field epifluorescence microscopy", J. Opt. Soc. Am. B 20, 554 (2003).

C. F. Bohren, D. R. Huffman, *Absorption and Scattering of Light by Small Particles* ; Wiley-VCH: Weinheim, Germany, 2004.

L. Bonacina, Y. Mugnier, F. Courvoisier, R. Le Dantec, J. Extermann, Y. Lambert, V. Boutou, C. Galez, J.-P. Wolf, "Polar Fe(IO3)3 nanocrystals as local probes for nonlinear microscopy", Appl. Phys. B 87, 399 (2007).

A Bouhelier, M. Berverhuis, and L. Novotny, "Near-Field Second-Harmonic Generation Induced by LocalField Enhancement," Phys. Rev. Lett. 90, 013903.1-013903.4 (2003).

R. W. Boyd, in *Nonlinear Optics*, Academic Press, 2nd ed., (2003).

S. Brasselet, V. Le Floc'h, F. Treussart, J.-F. Roch, J. Zyss, E. Botzung-Appert, and A. Ibanez, "In situ diagnosticsof the crystalline nature of single organic nanocrystals by nonlinear microscopy" Phys. Rev. Lett. 92, 207401-204405 (2004).

B. Broers, L. D. Noordam, and H. B. van Linden van den Heuvall, "Diffraction and focusing of spectralenergy in multiphoton processes," Phys. Rev. A 46, 2749-2756 (1992).

X. Brokmann, M.-V. Ehrensperger, J.-P. Hermier, A. Triller M. Dahan, "Orientational imaging and tracking of single CdSe nanocrystals by defocused", Chem. Phys. Lett. 406, 210 (2005).

B. C. Buchler, T. Kalkbrenner, C. Hettich, V. Sandoghdar, "Measuring the Quantum Efficiency of the Optical Emission of Single Radiating Dipoles Using a Scanning Mirror",Phys. Rev. Lett. 95, 063003 (2005).

R. Carminati, J.-J. Greffet, C. Henkel, J.-M. Vigoureux, "Radiative and non-radiative decay of a single molecule close to a metallic nanoparticle", Opt. Commun. 261, 368 (2006).

J. Chen, S. Machida, and Y. Yamanoto, "Simultaneous measurement of amplitude and phase in surface second-harmonic generation", Opt. Lett. 23, 676 (1998).
T. A. Driscoll, H. J. Hoffman, R. E. Stone, P. E. Perkins, "Efficient second-harmonic generation in KTP crystals", J. Opt. Soc. Am. B 3, 683 (1986).
N. Dudovich, D. Oron, and Y. Silberberg, "Single-pulse coherently controlled nonlinear Raman spectroscopy and microscopy," Nature 418, 512-514 (2002).
J. Extermann, L. Bonacina, F. Courvoisier, D. Kiselev, Y. Mugnier, R. Le Dantec, C. Glez, and J. -P. Wolf,"Nano-FROG: Frequency resolved optical gating by a nanometric object," Opt. Express 16, 10405-10411(2008)
J. B. Guild, C. Xu, and W. W. Webb, "Measurement of group delay dispersion of high numerical apertureobjective lenses using two-photon excited fluorescence," Appl. Opt. 36, 397-401 (1997).
G. Hansson, H. Karlsson, S.Wang, F. Laurell, "Transmission Measurements in KTP and Isomorphic Compounds", Appl. Opt. 39, 5058 (2000).
C. Hsieh, R. Grange, Y. Pu, D. Psaltis, "Three-dimensional harmonic holographic microcopy using nanoparticles as probes for cell imaging," Opt. Express 17, 2880 (2009)
J. C. Johnson, H. Yan, R. D. Schaller, P. B. Petersen, P. Yang, R. J. Saykally, "Near-Field Imaging of Nonlinear Optical Mixing in Single Zinc Oxide Nanowires", Nano Lett 2, 279 (2002).
A. V. Kachynski, A. N. Kuzmin, M. Nyk, I. Roy and P. N. Prasad, ?Zinc Oxide Nanocrystals for Nonresonant Nonlinear Optical Microscopy in Biology and Medicine,? J. Phys. Chem. C, 112, 10721 (2008)
K. Kemnitz, K. Bhattacharyya, J. M. Hicks, G. R. Pinto, K. B. Eisenthal, T. F. Heinz, "The phase of second-harmonic light generated at an interface and its relation to absolute molecular orientation", Chem. Phys. Lett. 131, 285 (1986).
S. Kurtz and T. Perry, "A powder technique for the evaluation of nonlinear optical materials," IEEE J.Quantum Electron. 4, 333-333 (1968).
F. Laurell, M.G. Roelofs, W.Bindloss, H.Hsiung, A. Suna, and J.D. Bierlein, "Detection of ferroelectric domain reversal in KTiOPO4 waveguides," J. Appl. Phys. 71, 4664 (1992)
V. Le Floc?h, S. Brasselet, J.-F. Roch, J. Zyss, "In Situ Diagnostics of the Crystalline Nature of Single Organic Nanocrystals by Nonlinear Microscopy" J. Phys. Chem. B 107, 12403 (2003).
L. Le Xuan, S. Brasselet, F. Treussart, J.-F. Roch, F. Marquier, D. Chauvat, S. Perruchas, C. Tard, T. Gacoin, "Balanced homodyne detection of second-harmonic generation from isolated subwavelength emitters", Appl. Phys. Lett. 89, 121118 (2006).
L. Le Xuan, C. Zhou, A. Slablab, D. Chauvat, C. Tard, S. Perruchas, T. Gacoin, P. Villeval, and J. -F.Roch, "Photostable Second-Harmonic Generation from a Single KTiOPO4 Nanocrystal for NonlinearMicroscopy," Small 4, 1332-1336 (2008).
J. P. Long, B. S. Simpkins, D. J. Rowenhorst, P. E. Pehrsson, "Far-field Imaging of Optical Second-Harmonic Generation in Single GaN Nanowires", Nano Lett. 7, 831 (2007).
V. V. Lozovoy, I. Pastirk, and M. Dantus, "Multiphoton intrapulse interference. IV. Ultrashort laser pulsespectral phase characterization and compensation," Opt. Lett. 29, 775-777 (2004).
D. Meshulach and Y. Silberberg, "Coherent quantum control of two-photon transitions by a femtosecondlaser pulse," Nature 396, 239-242 (1998).
L. Moreaux, O. Sandre, J. Mertz, "Membrane imaging by second-harmonic generation microscopy", J. Opt. Soc. Am. B 17, 1685 (2000).

Y. Nakayama, P. J. Pauzauskie, A. Radenovic, R. M. Onorato, R. J. Saykally, J. Liphardt, P. Yang, "Tunable nanowire nonlinear optical probe", Nature 447, 1098, (2007).

G. H. Patterson, D.W. Piston, "Photobleaching in Two-Photon Excitation Microscopy", Biophys. J. 78, 2159 (2000).

P. Rejmankova, J. Baruchel, P. Villeval, C. Saunal, "Characterization of large KTiOPO4 flux grown crystals by synchrotron radiation topography", J. of Crystal Growth 180, 85 (1997).

N. Sandeau, L. Le Xuan, C. Zhou, D. Chauvat, J.-F. Roch, S. Brasselet, "Defocused imaging of second harmonic generation from a single nanocrystal", Opt. Express 15, 16051 (2007).

Y. Shen, P. Markowicz, J.Winiarz, J. Swiatkiewicz, P. N. Prasad, "Nanoscopic study of second-harmonic generation in organic crystals with collection-mode near-field scanning optical microscopy", Opt. Lett. 26, 725 (2001).

Y. R. Shen, "Surface properties probed by second-harmonic and sum-frequency generation", Nature 337, 519 (1989).

M. I. Stockman, D. J. Bergman, C. Anceau, S. Brasselet, J. Zyss, "Enhanced Second-Harmonic Generation by Metal Surfaces with Nanoscale Roughness: Nanoscale Dephasing, Depolarization, and Correlations", Phys. Rev. Lett. 92, 057402 (2004).

R. Stolle, G. Marowsky, E. Schwarzberg, G. Berkovic, "Phase measurements in nonlinear optics", Appl. Phys. B, 63, 491 (1996) and Refs. therein.

R. L. Sutherland, *Handbook of Nonlinear Optics* , Dekker, New York, 1996 pp. 267.

F. Treussart, E. Botzung-Appert, N. T. Ha-Duong, A. Ibanez. J.-F. Roch, R. Pansu, "Second Harmonic Generation and Fluorescence of CMONS Dye Nanocrystals Grown in a Sol-Gel Thin Film", Chem. Phys. Chem. 4, 757 (2003).

F. Treussart, V. Jacques, E Wu, T. Gacoin, P. Grangier, J.-F. Roch, "Photoluminescence of single colour defects in 50ănm diamond nanocrystals", Physica B 376, 926 (2006).

H. Vanherzeele, and J. D. Bierlein, "Magnitude of the nonlinear-optical coefficients of KTiOPO4 ", Opt. Lett. 17,982-985 (1992).

W. S. Warren, R. Rabitz, and M. Daleh, "Coherent Control of Quantum Dynamics: The Dream Is Alive,"Science 259, 1581-1589 (1993).

A. M. Weiner, "Femtosecond pulse shaping using spatial light modulators," Rev. Sci. Instrum. 71, 1929-1960 (2000).

P. Wnuk and C. Radzewicz, "Coherent control and dark pulses in second harmonic generation," Opt.Commun. 272, 496-502 (2007).

P. Wnuk, L. Le Xuan, A. Slablab, C. Tard, S. Perruchas, T. Gacoin, J-F. Roch, D. Chauvat, and C. Radzewicz, "Coherent nonlinear emission from a single KTP nanoparticle with broadband femtosecond pulses", Optics Express, 17, 4652 (2009)

P. Xi, Y. Andegeko, L. R. Weisel, V. V. Lozovoy, and M. Dantus, "Greater Signal and LessPhotobleaching in Two-Photon Microscopy with Ultrabroad Bandwidth Femtosecond Pulses," Opt.Commun. 281, 1841-1849 (2008).

H. P. Yuen, V. W. S. Chan, "Noise in homodyne and heterodyne detection," Opt. Lett. 8, 177 (1983).

F. C. Zumsteg, J. D. Bierlein, T. E. Gier, "$K_xRb_{1-x}TiOPO_4$: A New Nonlinear Optical Material," J. Appl. Phys. 47, 4980 (1976).

IntechOpen

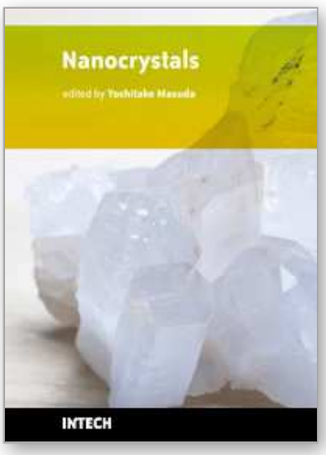

Nanocrystals

Edited by Yoshitake Masuda

ISBN 978-953-307-126-8
Hard cover, 326 pages
Publisher Sciyo
Published online 06, October, 2010
Published in print edition October, 2010

This book contains a number of latest research developments on nanocrystals. It is a promising new research area that has received a lot of attention in recent years. Here you will find interesting reports on cutting-edge science and technology related to synthesis, morphology control, self-assembly and application of nanocrystals. I hope that the book will lead to systematization of nanocrystal science, creation of new nanocrystal research field and further promotion of nanocrystal technology for the bright future of our children.

How to reference

In order to correctly reference this scholarly work, feel free to copy and paste the following:

Loc Le Xuan, Abdallah Slablab, Pawel Wnuk, Czeslaw Radzewicz, Dominique Chauvat and Jean-Francois Roch (2010). KTiOPO4 Single Nanocrystal for Second-Harmonic Generation Microscopy, Nanocrystals, Yoshitake Masuda (Ed.), ISBN: 978-953-307-126-8, InTech, Available from: http://www.intechopen.com/books/nanocrystals/ktiopo4-single-nanocrystal-for-second-harmonic-generation-microscopy

INTECH
open science | open minds

InTech Europe
University Campus STeP Ri
Slavka Krautzeka 83/A
51000 Rijeka, Croatia
Phone: +385 (51) 770 447
Fax: +385 (51) 686 166
www.intechopen.com

InTech China
Unit 405, Office Block, Hotel Equatorial Shanghai
No.65, Yan An Road (West), Shanghai, 200040, China
中国上海市延安西路65号上海国际贵都大饭店办公楼405单元
Phone: +86-21-62489820
Fax: +86-21-62489821

IntechOpen